



The toughness of mechanical metamaterials

Angkur Jyoti Dipanka Shaikeea^{1,5}, Huachen Cui^{2,3,5}, Mark O'Masta^{1,4}, Xiaoyu Rayne Zheng^{1,2,3}✉ and Vikram Sudhir Deshpande¹✉

Rapid progress in additive manufacturing methods has created a new class of ultralight mechanical metamaterials with extreme functional properties. Their application is ultimately limited by their tolerance to damage and defects, but an understanding of this sensitivity has remained elusive. Using metamaterial specimens consisting of millions of unit cells, we show that not only is the stress intensity factor, as used in conventional elastic fracture mechanics, insufficient to characterize fracture, but also that conventional fracture testing protocols are inadequate. Via a combination of numerical and asymptotic analysis, we extend the ideas of elastic fracture mechanics to truss-based metamaterials and develop a general test and design protocol. This framework can form the basis for fracture characterization in other discrete elastic-brittle solids where the notion of fracture toughness is known to break down.

Lightweight, three-dimensional micro- and nano-lattices represent a promising class of low-density materials ($<100\text{ kg m}^{-3}$) with numerous applications, such as thermal insulation¹, battery electrodes² and energy absorption³, to name a few. They achieve remarkable mechanical and functional properties^{4–6}, governed in part by the parent material and in part by their architecture, and hence are commonly referred to as mechanical metamaterials. Recently, additive manufacturing techniques, such as projection microstereolithography⁷ and two-photon lithography⁸, have led to the realization of polymeric⁴, metallic⁵ and ceramic⁹ metamaterials. Effective properties have also been defined for these materials, with extensive reporting of their modulus and compressive behaviour^{5,10–13}. As manufacturing processes scale up, resulting in the proliferation of metamaterials, an assessment of their tolerance to manufacturing defects and damage is critical. In continuum solids, the material property known as fracture toughness is used for such an assessment. However, an understanding and measurement of toughness in three-dimensional (3D) metamaterials has remained elusive, partly due to the inability so far to manufacture samples with a sufficient number of periodic unit cells^{14–17} so as to be able to generate the required crack tip K -field.

In a continuum elastic material, a stress distribution known as a K -field is established near the crack tip¹⁸, which is described by a single scalar parameter known as the stress intensity factor, K_I . Rapid, unstable crack advance will occur when $K_I = K_{Ic}$, where K_{Ic} is the fracture toughness of the material¹⁸. All previous work^{14–17,19–22} has assumed, a priori, that these ideas extend to truss-type 3D metamaterials and have used well-established experimental²³ and theoretical¹⁸ methods to estimate K_{Ic} . Here we show via experimental measurements and numerical analyses that fracture of such metamaterials cannot be described solely by K_{Ic} and also that standard measurement protocols, developed for continua such as metals and ceramics, are inappropriate for architected materials.

Our study used a stretch-dominated¹² metamaterial consisting of a network of struts where the nodes are arranged in a face-centred cubic (fcc) lattice: the so-called octet-truss^{13,24}. Fabrication of large 3D specimens, consisting of nearly 10 million periodic cells and cell sizes as small as $150\text{ }\mu\text{m}$, was accomplished using a large-area

projection microstereolithography system, where each layer is fabricated via a continuously moving projection so that curing occurs in subsections. This enables the creation of metamaterial specimens with millions of unit cells and homogeneous mechanical properties⁷. (See the Methods and Supplementary Fig. 1, as well as the Supplementary Information, including Extended Data Figs. 1 and 2, for details of imperfections and material properties.) The system utilizes a dynamic, coordinated optical scanning system to continuously project and scan two-dimensional (2D) slices onto an ultraviolet-curable photopolymer, to produce large-scale 3D parts with microscale resolutions. This enables us to manufacture specimens with embedded cracks and with a sufficient number of unit cells so as to develop a K -field and thereby perform a range of valid fracture toughness measurements. The results testify that the finite unit cell sizes restrict the development of singular stresses, with the consequence that K_{Ic} alone is an insufficient parameter to characterize fracture. Via a combination of measurements, including *in situ* X-ray computed tomography (XCT) observation and large-scale numerical simulations (with billions of degrees of freedom), we illustrate that a combination of K_I and the so-called T-stress fully characterizes the fracture mechanisms over a wide range of specimen densities, parent materials, cell sizes and crack sizes, as well as loading configurations.

Investigation of K_{Ic} as a fracture parameter

Cubic octet-truss specimens of dimension $2W=2H=2B=30\text{ mm}$ (W , width; H , height; B , breadth; Fig. 1a) were fabricated with trimethylolpropane triacrylate (TMPTA) as the parent material. This polymer is linear elastic with a modulus $E_s \approx 430\text{ MPa}$, and fails in a brittle manner with failure strength $\sigma_f \approx 11\text{ MPa}$ (failure strain $\epsilon_f \approx 0.025$); see Methods and Supplementary Fig. 2. The unit cell (Fig. 1a) of the octet-truss resembles an fcc microstructure, such that the octet-truss deforms primarily by axial stretching of the constituent struts¹². Specimens tested in this study had cell sizes in the range $0.15\text{ mm} \leq \ell \leq 0.75\text{ mm}$ and relative density $\bar{\rho}$ (that is, the density ratio between the metamaterial and its parent material) in the range $0.01 \leq \bar{\rho} \leq 0.10$. The largest strut diameter in the specimens tested is $2r_0 = 65\text{ }\mu\text{m}$ (Supplementary Table 1), which is much smaller than

¹Department of Engineering, University of Cambridge, Cambridge, UK. ²Advanced Manufacturing and Metamaterials Laboratory, Department of Mechanical Engineering, Virginia Polytechnical Institute and State University, Blacksburg, VA, USA. ³Advanced Manufacturing and Metamaterials Laboratory, Civil and Environmental Engineering, University of California, Los Angeles, CA, USA. ⁴HRL Laboratories, Malibu, CA, USA. ⁵These authors contributed equally: Angkur Jyoti Dipanka Shaikeea, Huachen Cui. ✉e-mail: rayne@seas.ucla.edu; vsd20@cam.ac.uk

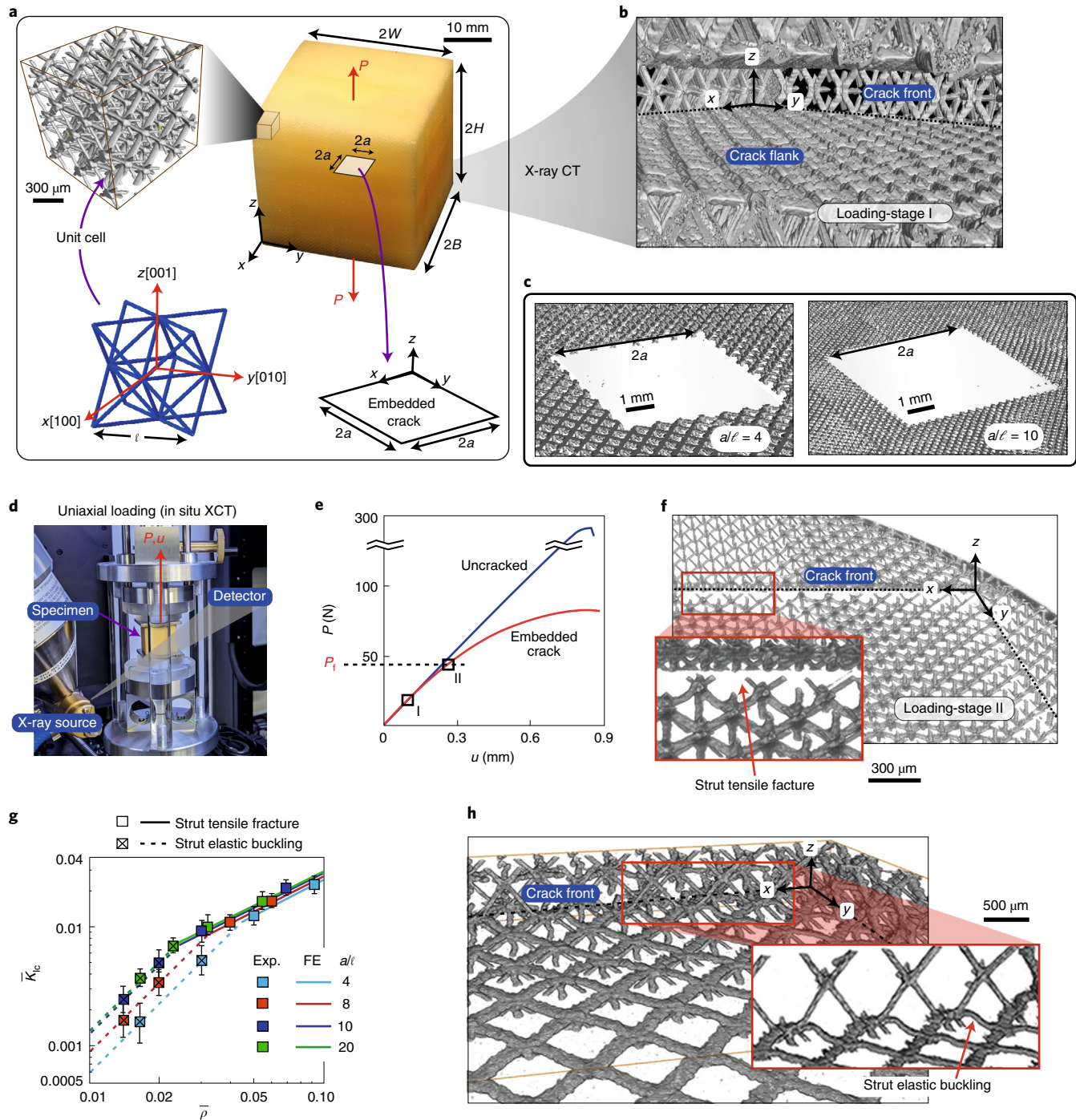


Fig. 1 | Failure under uniaxial tensile loading. **a**, Optical image of the cubic octet-truss specimen with an embedded square crack of side $2a$. Insets: XCT images of the octet-truss microstructure, unit cell and orientation and geometry of the embedded crack. **b,c**, XCT images of the crack front/flank at loading-stage I in **(b)** and cracks of fixed size $2a$ but with varying cell sizes ℓ as parameterized by a/ℓ (**c**). **d**, Tensile loading set-up, with in situ XCT imaging. **e**, Tensile load P versus displacement u response of the $\bar{\rho} = 0.08$ uncracked and cracked ($a/\ell = 10$) specimens. **f**, The crack front/flanks at K_c (loading-stage II in **e**). Inset: a magnified view of the failed crack front struts. **g**, Measured normalized toughness \bar{K}_{lc} versus relative density $\bar{\rho}$ (lines are FE predictions and symbols are measurements with error bars indicating variation over five test samples). **h**, XCT image for the $\bar{\rho} = 0.03$ and $a/\ell = 4$ specimen when failure is set by elastic buckling of crack front struts Inset: a magnified view of the buckled struts.

the transition flaw size of the TMPTA (Supplementary Information). Thus, tensile fracture of the struts in the octet-truss specimens occurs in a purely brittle manner with no associated inelastic deformation. The small cell size compared to specimen size implies that no microstructural features are visible via macroscale observations

of these specimens (Fig. 1a), and thus they resemble structure-free continua for which there exists a large and well-developed field of fracture mechanics¹⁸. A crack within a periodic truss metamaterial is a continuous array of broken nodal connections and here we consider such a sharp square crack of fixed size $2a=6\text{ mm}$ embedded

centrally in the specimen (Fig. 1a), with the crack corresponding to a missing layer of unit cells (Fig. 1b,c, Supplementary Fig. 3 and Supplementary Video 1). The global Cartesian coordinate system (x , y , z) is coincident with the [100], [010] and [001] directions, respectively, of the fcc microstructure, with the crack fronts also colinear with the x and y directions (Fig. 1a).

As a first step to characterize fracture, we conducted uniaxial tensile tests for loading in the z direction combined with an in situ XCT observation protocol (Fig. 1d and Methods) to monitor failure in the vicinity of the embedded crack. For a macroscopic tensile load P applied perpendicular to the crack plane (Fig. 1a), the mode I stress intensity factor K_I is given by

$$K_I = Y_1 \left(\frac{a}{W}, \frac{E_x}{G_{xy}}, \nu_{xy} \right) \frac{P}{4(WB)} \sqrt{\pi a} \quad (1)$$

where Y_1 is a calibration factor that depends on specimen geometry parameterized by a/W and ratios of the effective elastic constants (that is, Young's modulus E_x to shear modulus G_{xy} and Poisson's ratio ν_{xy}) of the octet-truss with cubic symmetry; see Supplementary Information for details of the calibration procedure for Y_1 and that Y_1 is approximately constant along the crack front in the octet-truss with cubic elastic symmetry. The fracture toughness K_{lc} is then defined as the value of K_I at load $P = P_f$ at which crack front struts fail as determined via in situ XCT observations. We fixed $a/W = 0.2$ for all measurements in line with most continuum fracture testing protocols (continuum mechanics specifies that K_{lc} calculated from a measured P_f is independent of crack size $2a$ when a/W is fixed). The load P versus displacement u for specimens with and without a crack are shown in Fig. 1e ($\bar{\rho} = 0.08$, $a/\ell = 10$). XCT images in Fig. 1f illustrate that the deviation in response of the cracked specimen to its uncracked counterpart is associated with the onset of tensile fracture of crack front struts, while P_f is defined as the load P at which crack front struts fail in the XCT observations, which also coincides with dP/du first reducing to ~95% of its initial value. We report measurements on specimens with cracks spanning over 8 to 40 unit cells, that is, $4 \leq a/\ell \leq 20$, where a/ℓ (which quantifies the number of unit cells over the crack flank; see Supplementary Fig. 4 and Supplementary Information) is varied by manufacturing specimens of varying cell sizes ℓ keeping the overall specimen and crack sizes fixed (Fig. 1c). Dimensional analysis^{16,17,19} dictates that $\bar{K}_{lc} \equiv K_{lc}/(\sigma_f \sqrt{\ell})$ is then solely a function of $\bar{\rho}$ and ϵ_f with the effect of ℓ normalized out (Fig. 1g). At high values of $\bar{\rho}$, the failure mode is tensile fracture of struts at the crack front (Fig. 1f and Supplementary Video 2) and K_{lc} scales linearly with $\bar{\rho}$, as is well established^{25,26} for the stretch-dominated octet-truss lattice. However, the scaling relationship changes to $\bar{\rho}^2$ at lower densities, as the failure mode switches to elastic buckling of struts at the crack front (Fig. 1h). Buckling of struts in an octet-truss subjected to tensile loading is well known¹³, but the presence of the crack exacerbates this failure mode in the vicinity of the crack. Although elastic buckling of struts does not necessarily result in strut fracture, it limits structural integrity. This is evidenced by the loss of load-carrying capacity and consequent nonlinearity of the P versus u response (Supplementary Fig. 5), similar to when struts fracture under tensile stresses. Hence, the deviation from linearity is used to define a toughness. More intriguing is the dependence of \bar{K}_{lc} on the number of unit cells in the crack, as parameterized via a/ℓ . The apparent toughness increases with increasing a/ℓ more prominently at lower relative densities, where toughness is set by strut elastic buckling. Such dependence of toughness on a/ℓ is excluded in continuum fracture mechanics and suggests that K_{lc} is inadequate to characterize the crack-based failure modes of octet-truss lattices, at least for cracks spanning less than 20 unit cells ($a/\ell < 10$); for $a/\ell \geq 10$, the dependence on a/ℓ becomes negligible in these uniaxial tensile experiments (Fig. 1g).

The unexpected a/ℓ dependence of \bar{K}_{lc} suggests a fundamental lack of understanding of the parameters that govern failure at crack fronts in metamaterials. To investigate further, we performed multi-axial loading measurements by applying a combination of axial load P in the z direction and in-plane equibiaxial loads Q in both the x and y directions (Fig. 2a, Supplementary Fig. 6 and Supplementary Information). Proportional loading experiments were conducted for tensile loading P while keeping the triaxiality $\lambda \equiv Q/P$ constant. The stress intensity factor K_I is independent of λ , and thus continuum elastic fracture mechanics require the measured toughness to be independent of λ . Measurements of \bar{K}_{lc} as a function of λ for two choices of $\bar{\rho}$ and a/ℓ to span the tensile fracture and elastic buckling failure modes (Fig. 2b) show a strong dependence of \bar{K}_{lc} on both λ and a/ℓ . This further confirms that \bar{K}_{lc} is an insufficient parameter to characterize failure of these metamaterials.

To help develop a physical understanding of the observations, we performed finite element (FE) simulations for both uniaxial and multiaxial loading cases, where every strut in the specimen is modelled (Fig. 2c and Methods). Typical calculations had in excess of 20 billion degrees of freedom. Predictions of \bar{K}_{lc} (Figs. 1g and 2b) and the corresponding failure modes (Fig. 2d–g) illustrate the fidelity of the model in capturing both tensile and elastic buckling failure modes. While the measured \bar{K}_{lc} is highly repeatable, the precise location of struts in elastic buckling varies from crack front (Fig. 2h) to crack flank (Fig. 2i and Supplementary Video 3) in nominally equivalent experiments. The difference in failure loads for the crack front and flank buckling modes (Fig. 2e,f) is predicted as less than 2% for the $\bar{\rho} = 0.03$ and $a/\ell = 4$ specimens, and this holds for all cases considered here. Thus, it is the inevitable small imperfections in the as-manufactured specimens set the precise buckling failure mode, thereby rationalizing the variability of buckling modes observed in the experiments (Figs. 1h and 2h,i). The fidelity of the FE predictions, where every strut within the specimen is discretely modelled, allows us to use these calculations to probe the apparent inadequacy of K_{lc} to characterize fracture.

Source of crack size and stress triaxiality dependence of K_{lc}
Fracture of elastic continua is well characterized by toughness K_{lc} , but here we have demonstrated that toughness for the octet-truss metamaterial depends on both λ and a/ℓ . Under plastic deformations, the stress triaxiality is known to influence fracture via the so-called T-stress. While plasticity is not operative in our experiments (TMPTA is elastic-brittle; Supplementary Fig. 2), the strong influence of stress triaxiality as parameterized by λ suggests that T-stresses might surprisingly influence the elastic fracture of the octet-truss.

An asymptotic analysis of an elastic continuum with cubic symmetry dictates that the stresses σ_{ij} around the crack tip, measured in the crack front coordinate system e_i (Fig. 3a), scale as

$$\tilde{\sigma}_{ij} \equiv \frac{\sigma_{ij}}{\sigma_f} = \bar{K}_I \left[\bar{r}^{-\frac{1}{2}} f_{ij}^l + \bar{T}_{11} \delta_{1i} \delta_{1j} + \bar{T}_{33} \delta_{3i} \delta_{3j} + \bar{T}_{13} \delta_{1i} \delta_{3j} + \mathcal{O}(\bar{r}^{\frac{1}{2}}) + \mathcal{O}(\bar{r}) + \dots \right] \quad (2)$$

where (r, θ) are the in-plane polar coordinates in a plane normal to the crack front, e_1 the direction formed by the intersection of the plane normal to the crack front and the crack plane and e_3 a direction tangential to the crack front within the crack plane. In equation (2) the normalized quantities are $\bar{r} \equiv r/\ell$, $\bar{K}_I \equiv K_I/(\sigma_f \sqrt{\ell})$ and $\bar{T}_{ij} \equiv T_{ij} \sqrt{\ell}/K_I$, with the non-dimensional function $f_{ij}^l(\theta, E_x/G_{xy}, \nu_{xy})$ governing the angular dependence of the singular stress terms, while T_{ij} are the so-called T-stress components and δ_{ij} is the Kronecker delta. The discreteness of the lattice (that is, a unit cell of size ℓ) implies that a mathematically sharp crack front cannot be defined. It is thus conceivable that fracture is governed

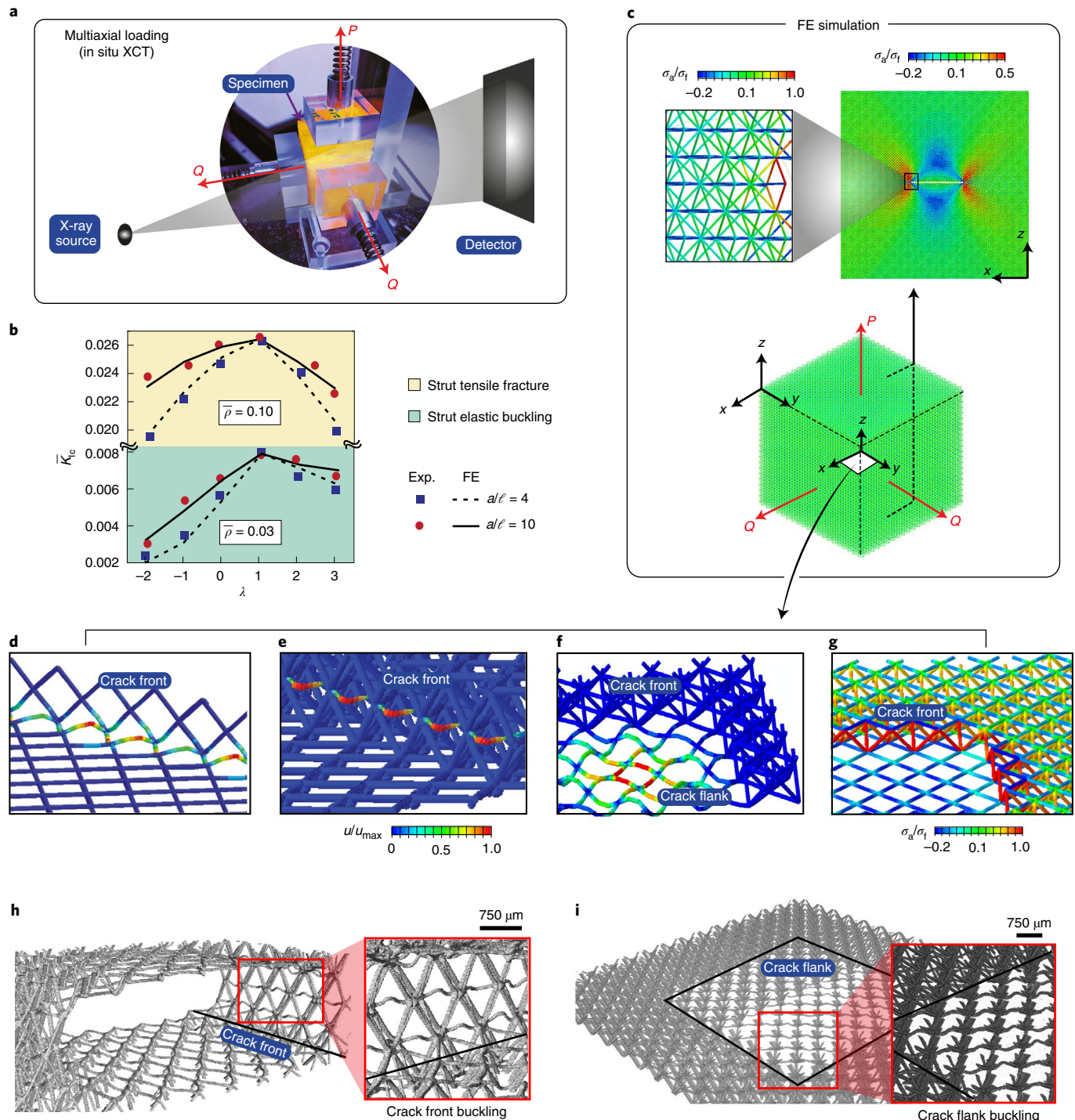


Fig. 2 | Failure under multiaxial loading. **a**, Multiaxial loading set-up with in situ XCT imaging. **b**, Summary of the measurements and FE predictions of \bar{K}_{Ic} as a function of the load triaxiality $\lambda \equiv Q/P$ for specimens that fail by strut fracture ($\bar{\rho} = 0.1$) and elastic strut buckling ($\bar{\rho} = 0.03$). Results are shown for two values of a/ℓ in both cases. **c**, FE modelling of the specimens. Insets: individual struts modelled as elastic solids and shaded by contours of the normalized axial stress σ_a/σ_t (σ_t is the strength of the parent solid TMPTA). **d–f**, FE predictions of the failure modes for loading with $\lambda = 1$. Failure set by elastic buckling of crack front (**d**, **e**) and crack flank struts (**f**) of the $\bar{\rho} = 0.03$ and $a/\ell = 4$ specimen. The predicted \bar{K}_{Ic} differs by 1% between the different eigenmodes in **d** and **e**, and by 2% between **e** and **f**. The struts are shaded by magnitude of normalized displacement u/u_{\max} . **g**, Distribution of normalized axial stresses σ_a/σ_t for the $a/\ell = 10$ and $\bar{\rho} = 0.10$ specimen ($\lambda = 1$) with crack tip struts predicted to undergo tensile fracture at K_{Ic} . **h**, **i**, XCT images for the $\bar{\rho} = 0.03$ and $a/\ell = 4$ specimen for loading with $\lambda = 1$ when failure is set by elastic buckling of crack front struts (**h**) and crack flank struts (**i**). Insets: magnified views of the buckled struts. The measured K_{Ic} between **h** and **i** differs by only 2%.

not only by the most singular term in the expansion (2), which scales with K_p , but also by the T-stress terms that are finite in the vicinity of $r = \ell$. To test this hypothesis in a simplistic setting, we

considered a one unit cell-thick slice through the octet-truss specimen (Fig. 3a) under plane-strain conditions and investigated the fields by performing an asymptotic analysis¹⁹. In particular, we

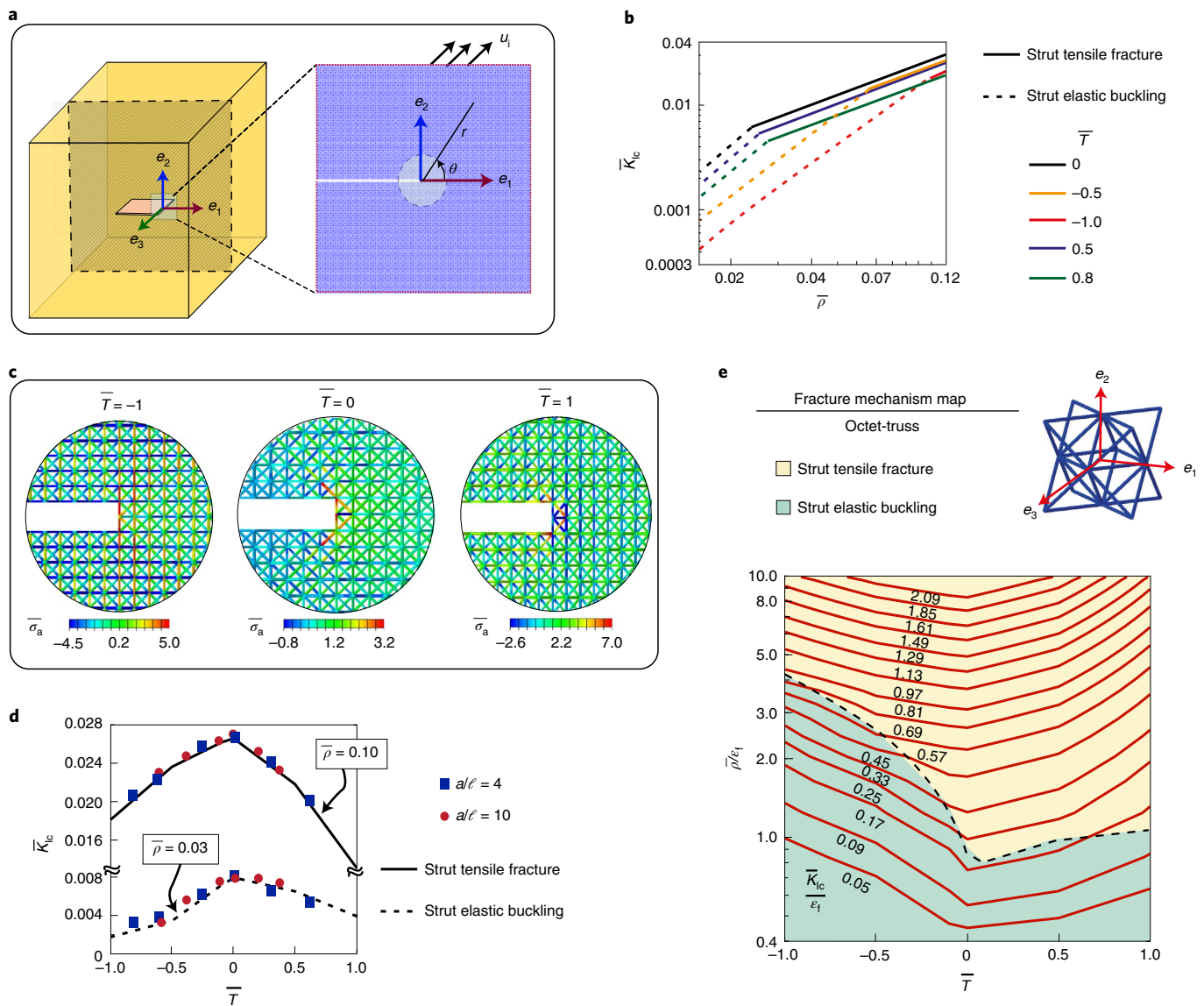


Fig. 3 | Fracture mechanism map. **a**, Sketch illustrating the crack front coordinate system and a 2D slice used in the asymptotic analysis. **b**, FE predictions showing the sensitivity of the asymptotic predictions of \bar{K}_{lc} to \bar{T} over a range of relative densities $\bar{\rho}$. **c**, FE predictions of normalized axial stress $\bar{\sigma}_a \equiv \sigma_a/(E_s \bar{\rho})$ around the crack tip for an applied $K_l/(E_s \sqrt{\ell}) = 0.01$ and three choices of the normalized T-stress \bar{T} . **d**, FE predictions and measurements from Fig. 2b replotted as a function of \bar{T} to illustrate that $\bar{\rho}$ and \bar{T} set \bar{K}_{lc} , with the effect of a/ℓ and λ both captured within \bar{T} . **e**, Fracture mechanism map of the octet-truss metamaterial, with axes of normalized T-stress \bar{T} and $\bar{\rho}/\epsilon_f$ and contours of \bar{K}_{lc}/ϵ_f . The strut tensile fracture and strut elastic buckling failure regimes are shaded.

considered a semi-infinite crack and imposed remote displacement boundary conditions consistent with only the K_l and T_{ij} terms in the expansion (2); Supplementary Information. In this plane-strain setting, with deformation restricted to the e_1-e_2 plane and the crack along the e_1 direction, $T_{13}=0$ and it suffices to specify the T-stress via $T=T_{11}$, as the plane-strain condition then requires $T_{33}=\nu_{xy}T$. Thus, loading is uniquely specified by the combination $(\bar{K}_l, \bar{T} \equiv T\sqrt{\ell}/K_l)$.

Predictions (Fig. 3b) of \bar{K}_{lc} in this plane-strain setting for \bar{T} in the range $-1 \leq \bar{T} < 1$ are similar to the embedded crack 3D case, with fracture for high values of $\bar{\rho}$ set by tensile fracture of the struts, and the failure mode transitioning to elastic strut buckling at lower $\bar{\rho}$. These generalized 2D results are not only qualitatively consistent with the 3D measurements but also quantitatively very similar (observe the axes scales in Figs. 1g and 3b). Moreover, the

strong effect of \bar{T} on the predictions is analogous to that of λ , in the sense that \bar{K}_{lc} decreases with increasing $|\bar{T}|$ for a fixed $\bar{\rho}$. To understand this influence of \bar{T} , we performed a stress analysis and show the axial stress distributions (Fig. 3c) in struts around the crack tip for an applied $K_l/(E_s \sqrt{\ell}) = 0.01$ and three choices of \bar{T} . The axial stresses σ_a are normalized as $\bar{\sigma}_a \equiv \sigma_a/(E_s \bar{\rho})$ so that $\bar{\sigma}_a$ in Fig. 3c is independent of $\bar{\rho}$. Both tensile and compressive axial loads develop in struts around the crack tip, and hence failure can be governed by either strut tensile fracture or elastic buckling. The stress analysis illustrates that both maximum tensile and compressive stresses $\bar{\sigma}_a$ increase with increasing $|\bar{T}|$. This strong influence of \bar{T} is a consequence of the discreteness of the microstructure, which means that the second term (non-singular) in the asymptotic expansion (2) cannot be neglected, with \bar{T} strongly influencing the fracture mechanisms.

A fracture mechanism map

The asymptotic analysis suggests that T-stress effects are essential in developing a fracture criterion for the octet-truss metamaterial. But can the T-stress explain both the observed triaxiality λ and a/ℓ dependence of \bar{K}_{lc} ? The calibration analysis in equation (1) is extended to determine the T-stress for a mathematically sharp crack embedded in a 3D anisotropic elastic continuum (Supplementary Fig. 7). Using the crack front coordinate system e_i (Fig. 3a) and labelling $T = T_{11}$, we define $\bar{T} \equiv \hat{T}\sqrt{\ell/a}$, where $\hat{T} = T\sqrt{a}/K_1$ is a calibration constant for the T-stress, commonly known as the biaxiality ratio. The calibration of \hat{T} for our cubic specimen with an embedded square crack gives (Supplementary Information)

$$\bar{T} \approx \frac{\sqrt{\pi}}{2.2} (\lambda - 1) \sqrt{\frac{\ell}{a}} \quad (3)$$

and thus \bar{T} is a function of both λ and a/ℓ . The data (measurements and FE predictions) of Fig. 2b are replotted (Fig. 3d) using an x axis of \bar{T} given by equation (3) rather than λ . For a given $\bar{\rho}$, the data for both values of a/ℓ collapse onto a unique curve demonstrating that both the observed a/ℓ and λ dependence of \bar{K}_{lc} is in fact a T-stress effect. Thus, varying λ is equivalent to changing a/ℓ in terms of the influence on the effective toughness. These findings can be summarized in the form of a fracture mechanism map (Fig. 3e), where the y axis is the material property $\bar{\rho}/\varepsilon_f$ while the x axis is the structural parameter \bar{T} set by a combination of a/ℓ and λ (equation (3)). These structural and material parameters set the operating point on the map, from which we can read off the normalized toughness $\bar{K}_{lc}/\varepsilon_f$; we emphasize that this map is valid for an octet-truss metamaterial made from any elastic parent material irrespective of its failure strain ε_f (see Supplementary Information for a discussion of the normalizations used in Fig. 3e so as to make it valid for all ε_f). The failure regimes (strut elastic buckling and strut tensile fracture) are shaded, and we observe that the transition between the failure modes is strongly dependent on \bar{T} . This procedure to generate fracture mechanism maps is independent of topology, with examples for a range of bending- and stretching-dominated topologies provided in Extended Data Fig. 3 and an associated design protocol in Extended Data Fig. 4 (also see the discussion in the Supplementary Information).

The reversal of plane-strain and plane-stress toughness

A thick specimen with a through-thickness crack is conventionally used to evaluate the thickness-independent plane-strain fracture toughness²³. This measured value is typically quoted as a material property since the plane-strain toughness is lower than the plane-stress toughness (thin specimens) in standard continuum solids²⁷. (Fracture initiates within the specimen where plane-strain conditions prevail rather than on the specimen surfaces where the conditions resemble plane-stress, and the toughness is higher.) To date all fracture tests on metamaterials have used through-thickness cracks^{14–17}, but it remains unclear whether the underlying assumption of the plane-stress toughness exceeding the plane-strain toughness remains valid in these materials. If not, these tests have not measured the plane-strain toughness.

To investigate the use of through-thickness cracked specimens for the measurement of toughness, we considered centre-cracked tension (CCT) specimens (Fig. 4a) of in-plane dimensions $2W=2H=35$ mm. These specimens can be viewed as a slice through the midsection of the 3D embedded crack specimen (Fig. 3a). The thickness $2B$ of the specimens (which is in the [010] direction) was varied over $\ell \leq 2B \leq 100\ell$ to examine the plane-stress and plane-strain limits. Toughness K_Q (toughness inferred in this way is denoted as K_Q , as it is unclear whether it equals the plane-strain limit) is calculated using equation (1) with Y_1 recalibrated for the CCT specimens (Supplementary Information). Measurements of

\bar{K}_Q ($\bar{K}_Q \equiv K_Q/(\sigma_f\sqrt{\ell})$) versus $\bar{\rho}$ for two choices of a/ℓ (Fig. 4b) reveal a scaling behaviour very similar to the embedded crack specimens (Fig. 1g), although the sensitivity to a/ℓ is milder. The corresponding FE predictions show excellent agreement with measurements (Fig. 4b) and the XCT observations (Fig. 4c–e for the $2B = 1\ell$ specimen and Fig. 4f–h for the $2B = 100\ell$ specimen), which reveal that strut tensile fracture and strut elastic buckling are again the two operative failure modes. Intriguingly \bar{K}_Q is insensitive to thickness over $\ell \leq 2B \leq 100\ell$. This surprising observation is complemented by the fact that \bar{K}_Q is lower than \bar{K}_{lc} as measured from the embedded crack specimen for a given a/ℓ (results from Fig. 1g reproduced in Fig. 4b). This is all the more puzzling since \bar{K}_Q , which is the toughness of the $2B = \ell$ specimen, can be interpreted as the plane-stress toughness, while the embedded crack \bar{K}_{lc} measurements have no specimen surface effects and hence are representative of a plane-strain toughness. Thus, unlike conventional continuum materials the plane-stress toughness is lower than the plane-strain toughness for the octet-truss metamaterial. To understand this reversal, observe that failure even for the $2B = 100\ell$ specimen is dominated by failure of surface struts (Fig. 4g,h and Supplementary Video 4). FE predictions of the tensile and compressive axial stresses in the struts across the specimen thickness for the $2B = 100\ell$ specimen (Fig. 4a) confirm that both the compressive and tensile strut stresses are a maximum at the surface. These high surface stresses result from the surface nodes of the metamaterial being ‘unbalanced’; that is, struts are absent on one side causing higher stresses to build up in surface struts, resulting in their premature failure. In a specimen with a through-thickness crack, such free surfaces are always present irrespective of the specimen thickness, and thus fracture initiation is surface dominated. Therefore, two distinct types of characteristic toughness exist for architected materials: one for through-thickness or surface flaws and another for embedded flaws. The equivalent of a plane-strain toughness can only be measured via an embedded crack specimen that eliminates surface effects.

Outlook

Existing fracture analyses of elastic metamaterials^{16,17,19–22} have, *a priori* (and without subsequent experimental validation), assumed that the stress intensity factor is sufficient to characterize fracture, and then used FE calculations to develop scaling laws for the toughness. Such scaling can also be extracted from our measurements and analyses. For example, in the absence of a T-stress (that is, $\bar{T}=0$), our 3D embedded crack data suggest that the normalized toughness \bar{K}_{lc} scales as

$$\bar{K}_{lc} = \begin{cases} \alpha_0 \bar{\rho} & \text{for } \bar{\rho} \geq \frac{\alpha_0}{\beta_0} \varepsilon_f \\ \frac{\beta_0}{\varepsilon_f} \bar{\rho}^2 & \text{otherwise,} \end{cases} \quad (4)$$

where $\alpha_0=0.31$ and $\beta_0=0.33$, with tensile strut fracture being the operative failure mode for $\bar{\rho} \geq (\alpha_0/\beta_0)\varepsilon_f$. Here we have shown that such scaling laws cannot be used to predict fracture in components made from the octet-truss metamaterial, as α_0 and β_0 are dependent on the number of unit cells over the crack flank, as parameterized by a/ℓ and the imposed stress triaxiality λ . The effect of both a/ℓ and λ is captured via a single parameter, \bar{T} , which is related to the so-called T-stress in the asymptotic expansion of the crack tip fields. Unlike in 2D planar networks²⁶, the T-stress effect is shown to have a very large effect for a wide range of 3D metamaterials, with stress triaxiality effects amplifying the role of T-stresses in governing fracture. The T-stress is a non-singular term, which is neglected in continuum elastic fracture as fracture is a highly localized process that is dominated by singular stresses, which scales with the stress intensity factor K_I . However, the discreteness of the octet-truss metamaterial implies that a mathematically sharp

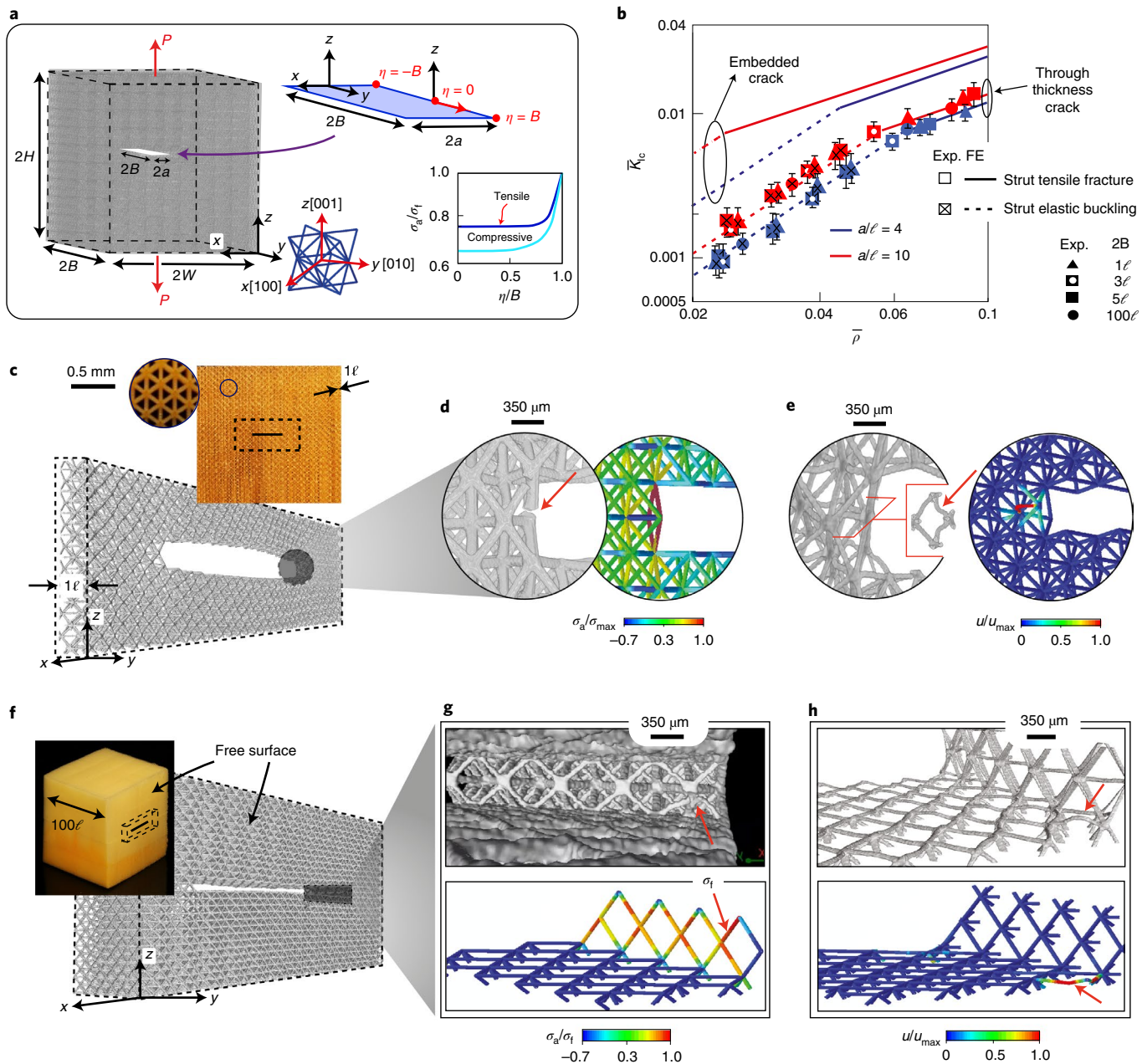


Fig. 4 | Through-thickness cracks. **a**, Sketch illustrating tensile loading of a specimen of thickness $2B$ with a through-thickness crack (CCT geometry). FE predictions of the variation of normalized axial strut stresses σ_a/σ_{\max} for struts along the crack front (the maximum tensile and compressive stresses are plotted in each unit cell along the crack front) are included in the inset, which also illustrates the local axis η along the crack front with $\eta=0$ at the midplane of the specimen and $\eta=\pm B$ on the specimen free surfaces. **b**, FE predictions and measurements (error bars indicating variation over five tests) of \bar{K}_{Ic} versus \bar{p} for specimens of different thicknesses $2B$. In each case, the results are shown for two values of a/ℓ , with the embedded crack results reproduced from Fig. 1g. **c**, XCT image of a portion of the $2B = \ell$ specimen. Inset: optical image of the specimen along with a magnified view of the microstructure (scale bar refers to inset). **d,e**, XCT images and FE predictions of the crack tip state at K_{Ic} in the $a/\ell = 10$ specimen illustrating the tensile fracture ($\bar{p} = 0.10$) (**d**) and elastic strut buckling ($\bar{p} = 0.03$) (**e**) failure modes. The FE predictions show distributions of the normalized axial stress σ_a/σ_{\max} and the normalized displacements u/u_{\max} in **d** and **e**, respectively, with the maximum taken over all struts in the specimen. **f**, XCT image of a portion of the $2B = 100\ell$ specimen, with $a/\ell = 10$ showing the free surface and five unit cells along the thickness. Inset: optical image of the specimen with the dashed cuboid marking the region of the XCT image. **g,h**, The corresponding FE predictions and XCT observations show that failure by tensile strut fracture ($\bar{p} = 0.10$) (**g**) and elastic strut buckling ($\bar{p} = 0.03$) (**h**) occurs on the specimen free surfaces.

crack is not present, and hence a strut that undergoes either tensile fracture or elastic buckling failure is at finite distance from the ill-defined crack front (Supplementary Information). In such a scenario, the non-singular T-stress terms become of similar order to

the K_I terms, creating the need for an enrichment of conventional elastic fracture mechanics to describe fracture of elastic metamaterials irrespective of their microstructure. Another consequence of the discreteness of the microstructure is the inadequacy of

conventional fracture testing protocols to measure material properties that describe fracture of 3D metamaterials. Specifically, contrary to all reported toughness measurements^{16,17}, the equivalent of a plane-strain toughness in 3D metamaterials cannot be measured using standard through-thickness cracked specimens, but rather crack specimens that eliminate surface effects. Nevertheless, since surface flaws are more detrimental compared to embedded flaws, measurement of toughness with through-thickness specimens will give a safe design envelope.

Our findings lead to revising the basic concepts of the fracture of elastic materials that have hitherto been restricted to the notion of a fracture toughness, and thereby establish the fundamental laws of failure in metamaterials. While T-stress effects have been reported in inelastic materials^{28–32} when the size of the damage process zone is comparable to the crack size, no such finite process zone exists in elastic mechanical metamaterials (Extended Data Fig. 5). This is also clear from the fact that the transition flaw size of the parent solid (TMPTA) is nearly 20 times the largest strut diameter of the metamaterials we have investigated (Supplementary Information). Rather, in elastic metamaterials, T-stress effects play an important role due to the discreteness of the microstructure.

The framework developed in this work hinges on the concept of a fracture mechanism map and we have shown this idea holds for other classes of truss-based metamaterials covering a range of anisotropies, deformation mechanisms and loading scenarios. Such maps can readily be used by designers to evaluate failure in different applications at negligible computational cost compared to modeling the microstructural details of the metamaterial.

Online content

Any methods, additional references, Nature Research reporting summaries, source data, extended data, supplementary information, acknowledgements, peer review information; details of author contributions and competing interests; and statements of data and code availability are available at <https://doi.org/10.1038/s41563-021-01182-1>.

Received: 20 January 2021; Accepted: 2 December 2021;

Published online: 7 February 2022

References

1. Valdevit, L., Pantano, A., Stone, H. A. & Evans, A. G. Optimal active cooling performance of metallic sandwich panels with prismatic cores. *Int. J. Heat Mass Transf.* **49**, 3819–3830 (2006).
2. Chung, D. D. L. *Composite Materials for Electrical Applications. Composite Materials: Science and Applications* (Springer, 2003).
3. Tancogne-Dejean, T., Spierings, A. B. & Mohr, D. Additively-manufactured metallic micro-lattice materials for high specific energy absorption under static and dynamic loading. *Acta Mater.* **116**, 14–28 (2016).
4. Zheng, X. et al. Ultralight, ultrastiff mechanical metamaterials. *Science* **344**, 1373–1377 (2014).
5. Zheng, X. et al. Multiscale metallic metamaterials. *Nat. Mater.* **15**, 1100–1106 (2016).
6. Bauer, J., Schroer, A., Schwaiger, R. & Kraft, O. Approaching theoretical strength in glassy carbon nanolattices. *Nat. Mater.* **15**, 438–443 (2016).

7. Zheng, X. et al. Design and optimization of a light-emitting diode projection micro-stereolithography three-dimensional manufacturing system. *Rev. Sci. Instrum.* **83**, 125001 (2012).
8. Cabrini, S. & Kawata, S. (eds) *Nanofabrication Handbook* (CRC Press, 2012).
9. Eckel, Z. C. et al. Additive manufacturing of polymer-derived ceramics. *Science* **351**, 58–62 (2016).
10. Meza, L. R. et al. Resilient 3D hierarchical architected metamaterials. *Proc. Natl Acad. Sci. USA* **112**, 11502–11507 (2015).
11. Kooistra, G. W., Deshpande, V. S. & Wadley, H. N. G. Hierarchical corrugated core sandwich panel concepts. *J. Appl. Mech.* **74**, 259–268 (2007).
12. Deshpande, V. S., Ashby, M. F. & Fleck, N. A. Foam topology: bending versus stretching dominated architectures. *Acta Mater.* **49**, 1035–1040 (2001).
13. Deshpande, V. S., Fleck, N. A. & Ashby, M. F. Effective properties of the octet-truss lattice material. *J. Mech. Phys. Solids* **49**, 1747–1769 (2001).
14. Montemayor, L. C., Wong, W. H., Zhang, Y. W. & Greer, J. R. Insensitivity to flaws leads to damage tolerance in brittle architected meta-materials. *Sci. Rep.* **6**, 20570 (2016).
15. Gu, H. et al. Fracture of three-dimensional lattices manufactured by selective laser melting. *Int. J. Solids Struct.* **180**, 147–159 (2019).
16. O'Masta, M. R., Dong, L., St-Pierre, L., Wadley, H. N. G. & Deshpande, V. S. The fracture toughness of octet-truss lattices. *J. Mech. Phys. Solids* **98**, 271–289 (2017).
17. Liu, Y., St-Pierre, L., Fleck, N. A., Deshpande, V. S. & Srivastava, A. High fracture toughness micro-architected materials. *J. Mech. Phys. Solids* **143**, 104060 (2020).
18. Anderson, T. L. *Fracture Mechanics: Fundamentals and Applications* 4th edn (CRC Press, 2017).
19. Tankasala, H. C., Deshpande, V. S. & Fleck, N. A. 2013 Koiter Medal Paper. Crack-tip fields and toughness of two-dimensional elastoplastic lattices. *J. Appl. Mech.* **82**, 091004 (2015).
20. Huang, J. S. & Lin, J. Y. Mixed-mode fracture of brittle cellular materials. *J. Mater. Sci.* **31**, 2647–2652 (1996).
21. Huang, J. S. & Gibson, L. J. Fracture toughness of brittle honeycombs. *Acta Metall. Mater.* **39**, 1617–1626 (1991).
22. Hsieh, M. T., Deshpande, V. S. & Valdevit, L. A versatile numerical approach for calculating the fracture toughness and R-curves of cellular materials. *J. Mech. Phys. Solids* **138**, 103925 (2020).
23. ASTM E1820 Standard Test Method for Measurement of Fracture Toughness (ASTM International, 2009).
24. Fuller R. B. Octet truss. US Patent 2,986,241 (1961).
25. Fleck, N. A., Deshpande, V. S. & Ashby, M. F. Micro-architected materials: past, present and future. *Proc. R. Soc. A* **466**, 2495–2516 (2010).
26. Fleck, N. A. & Qiu, X. The damage tolerance of elastic–brittle, two-dimensional isotropic lattices. *J. Mech. Phys. Solids* **55**, 562–588 (2007).
27. ASTM E399-74 Standard Method of Test for Plane-Strain Fracture Toughness of Metallic Materials (ASTM International, 1997).
28. Bažant, Z. P. & Planas, J. *Fracture and Size Effect in Concrete and Other Quasibrittle Materials* (Routledge, 2019).
29. Nguyen, H. et al. New perspective of fracture mechanics inspired by gap test with crack-parallel compression. *Proc. Natl Acad. Sci. USA* **117**, 14015–14020 (2020).
30. O'Dowd, N. P. & Shih, C. F. Family of crack-tip fields characterized by a triaxiality parameter—I. Structure of fields. *J. Mech. Phys. Solids* **39**, 989–1015 (1991).
31. O'Dowd, N. P. & Shih, C. F. Family of crack-tip fields characterized by a triaxiality parameter—II. Fracture applications. *J. Mech. Phys. Solids* **40**, 939–963 (1992).
32. Betegón, C. & Hancock, J. W. Two-parameter characterization of elastic-plastic crack-tip fields. *J. Appl. Mech.* **58**, 104–110 (1991).

Publisher's note Springer Nature remains neutral with regard to jurisdictional claims in published maps and institutional affiliations.

© The Author(s), under exclusive licence to Springer Nature Limited 2022, corrected publication 2022

Methods

Materials. The octet-truss metamaterial specimens were fabricated using the liquid monomer TMPTA (CAS 15628-89-5). The TMPTA was mixed with 1-phenylazo-2-naphthol (Sudan 1; CAS 842-07-9) photo-absorber to adjust the light penetration depth and phenylbis(2,4,6-trimethylbenzoyl)phosphine oxide (Irgacure 819), which served as a photo-initiator. The resulting solid material had a tensile failure strength of $\sigma_t \approx 11$ MPa and a Young's modulus, $E, \approx 430$ MPa for specimens with dimensions of the order of millimetre down to the micrometre scale representative of single struts within the octet-truss specimens (Fig. 1a). Nano-indentation tests were also conducted on single struts extracted from the printed specimens. The solid material modulus inferred from these tests varied by less than 5% for indentation carried out over a wide range of orientations, thereby confirming the isotropy of the as-printed material. The key advantage of TMPTA is that it has a linear elastic-brittle tensile response and a low strain-rate sensitivity (less than 20% change in modulus and fracture strength over three decades of strain rate).

Fabrication. In conventional large-area projection stereolithography (SLA), each layer is printed in a single projection with heat dissipation limited to peripheral cooling. This results in entrapment of heat in the central region, especially for large exposure areas (Supplementary Fig. 1a). Before heat is fully dissipated, the exposure of the next layer starts, and heat accumulates as layer number increases, making the polymerization highly non-uniform within the large printing area. The printed part thus suffers from non-uniform mechanical properties. To overcome this drawback, our fabrication method (Supplementary Fig. 1b) used a moving projection SLA technique where curing occurs in subsections that are exposed by a continuously moving projection (Supplementary Fig. 1c). There is thus less heat generated compared to exposing the entire cross-section and this results in more uniform polymerization compared to conventional SLA. Additionally, the moving projection means that heat is continuously dissipated with minimal accumulation. This unique method allows the production of large-scale parts (100 mm in overall size) with micrometre-scale resolution, low level of imperfections and spatially uniform mechanical properties, as validated in our experiments (Extended Data Figs. 1 and 2).

Experimental methodology. Postfabrication, the specimens were not exposed to any direct light before the mechanical measurements, which were performed within two weeks. The minimal photo-absorption postfabrication implied minimal spatial variability within the specimen, as confirmed via a series of mechanical tests (Supplementary Information). In any case there is minimal light penetration into the 3D specimens consisting of millions of unit cells, with the mechanical properties of the fabricated samples that are exposed to ambient light for more than 100 weeks showing minimal differences compared to those tested within two weeks of fabrication. Custom experimental rigs (Fig. 1d and Supplementary Fig. 6) were designed and fabricated to perform uniaxial (Fig. 1d) and multiaxial loadings (Fig. 2a) with in situ XCT observations. Specimens were first scanned in the as-manufactured state for quality checks, and then relative densities were computed using volume analysis available in the commercial software VGStudio Max v.3.4. Two different scan protocols were followed: quick scan (15 min acquisition time) and long scan (50 min) for in situ observations and analysis, respectively (details in Supplementary Information, Section C). A typical test involved 10–15 quick scans acquired at regular intervals along a measured load–displacement curve (Fig. 1e). The crack tip and crack flank conditions were monitored to detect the first event of failure (tensile fracture or strut buckling) around the crack front and flanks. The XCT images shown in Figs. 1, 2 and 4 and Supplementary Fig. 5 (and Supplementary Videos 1–4) were acquired using the long scan protocol with a $10\text{ }\mu\text{m} \times 10\text{ }\mu\text{m} \times 10\text{ }\mu\text{m}$ effective voxel size. To avoid XCT artefacts, beam energies were maintained below 10 W and only geometrical magnification was employed.

FE calculations. Three-dimensional FE calculations were performed in the commercial package ABAQUS, using linear elastic material properties (details

in Supplementary Information). The geometry of the specimens with embedded and through-thickness cracks used in the calculations was identical to the model used to 3D print the test specimens. Each strut in the octet-truss microstructure was represented by Timoshenko beam elements (B31 in the ABAQUS notation) with a circular cross-section of radius r_0 and length of $\ell/\sqrt{2}$: the radius r_0 is related to the relative density via $\bar{\rho} \equiv 6\sqrt{2}\pi (r_0/b)^2$. Each strut was discretized via 100 B31 elements in a region of leading dimension $2a$ around the crack (to accurately capture the crack tip fields), while further away from the crack each strut was discretized by only three elements (mesh convergence studies confirmed the accuracy of the discretization). This implied that the FE calculations had up to a billion degrees of freedom. Uniaxial and multiaxial loading (at fixed $\lambda \equiv Q/P$) was applied by imposing monotonically increasing forces on the FE nodes on the specimen surfaces, with all nodes on a given surface subjected to equal forces. Two types of analyses were conducted: (1) to investigate failure by strut tensile fracture, the specimens were loaded to failure load $P = P_T$ until a strut (typically in the close vicinity of the crack) attained the critical axial tensile stress σ_b ; (2) for the buckling failure mode, the eigenvalues were calculated for the imposed loading and the failure load P_B set equal to the lowest eigenvalue. The operative failure mode is the one associated with the lowest failure load and hence $P_f = \min(P_T, P_B)$ with K_{lc} then calculated by setting $P = P_f$ in equation (1). Details of the asymptotic calculations (Fig. 3) are provided in Supplementary Section E.

Data availability

All data are available in the main text or the supplementary materials.

Acknowledgements

We acknowledge funding from the Office of Naval Research (N00014-18-1-2658 and N00014-20-1-2504:P00001). H.C. and X.Z. also thank the NSF (2001677) and Air Force Office of Scientific Research (FA9550-18-1-0299) for funding support. A.J.D.S. is supported by the Cambridge-India Ramanujan scholarship from the Cambridge Trust and the SERB (Government of India). A.J.D.S. and V.S.D. thank S. R. Marshall and G. Smith for their help and support in the laboratory.

Author contributions

V.S.D., X.Z. and M.O.M. conceived and designed the research. H.C. developed the 3D printing platform, fabricated the octet-truss specimens and performed experiments. V.S.D. and A.J.D.S. designed the experiments (in situ XCT with multiaxial loading for fracture toughness measurements, digital volume correlation and imperfection analysis from XCT dataset) and the analytical formulations. A.J.D.S. performed these experiments, the numerical calculations and data analysis. V.S.D. and A.J.D.S. wrote the first draft of the manuscript. All authors participated in revising the manuscript, discussion and interpretation of the data.

Competing interests

The authors declare no competing interests.

Additional information

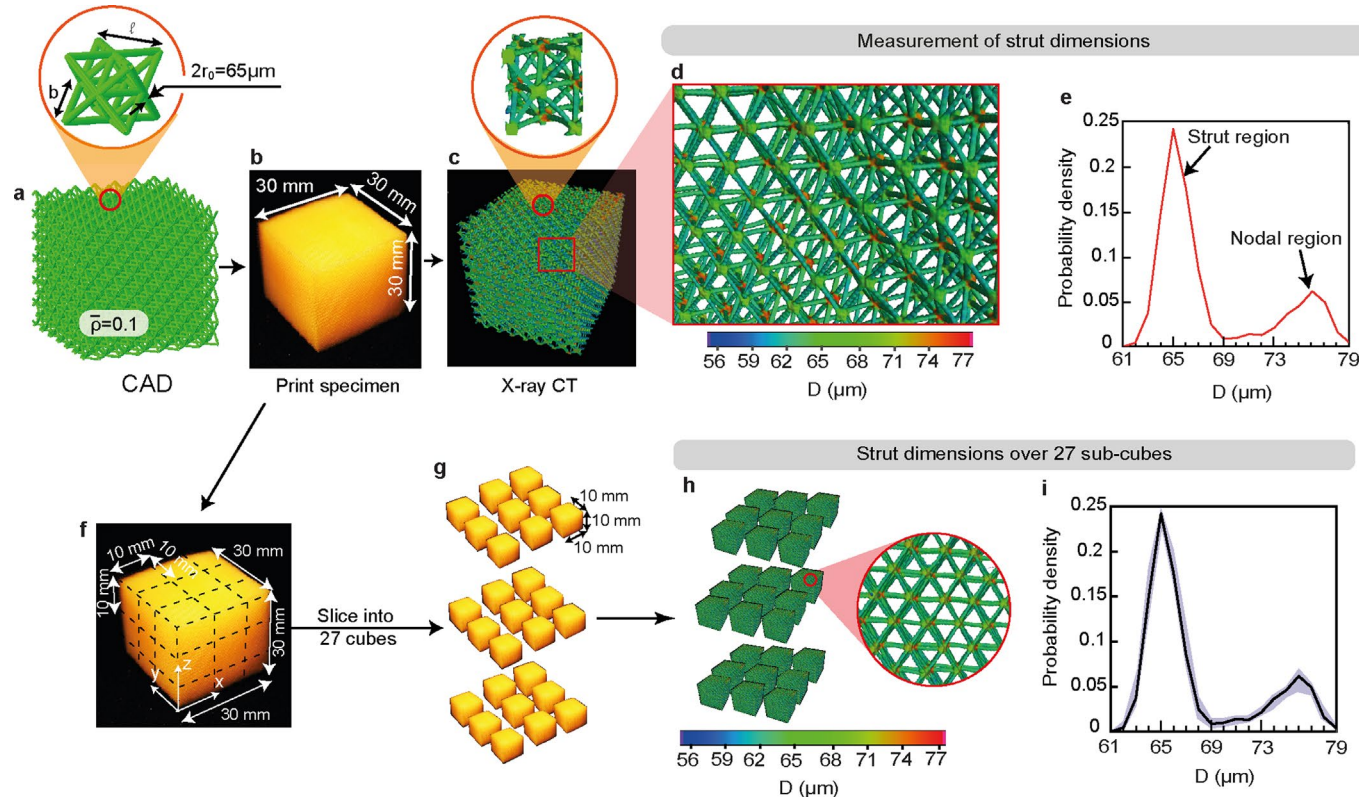
Extended data is available for this paper at <https://doi.org/10.1038/s41563-021-01182-1>.

Supplementary information The online version contains supplementary material available at <https://doi.org/10.1038/s41563-021-01182-1>.

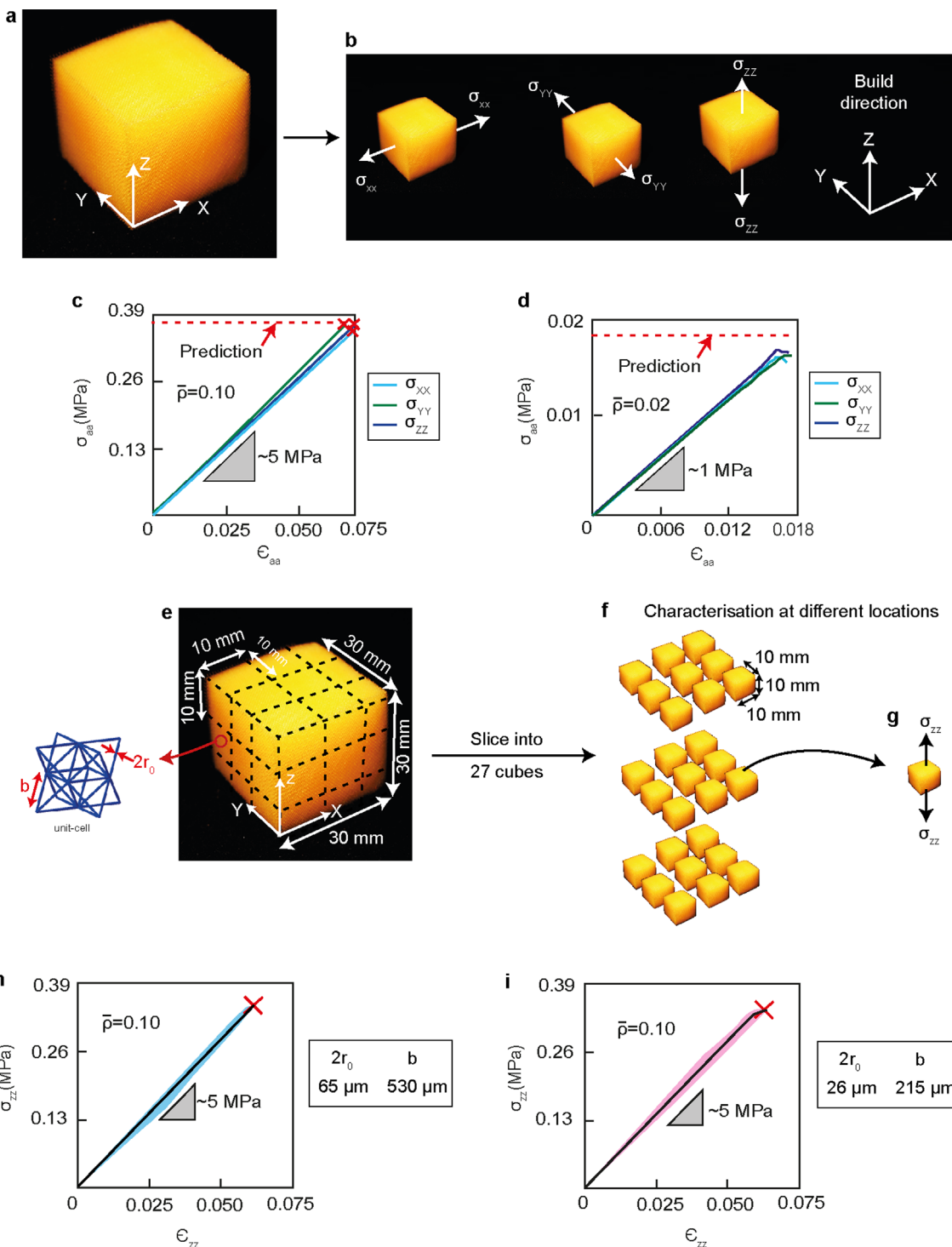
Correspondence and requests for materials should be addressed to Vikram Sudhir Deshpande.

Peer review information *Nature Materials* thanks Bin Liu, Yang Lu and the other, anonymous, reviewer(s) for their contribution to the peer review of this work.

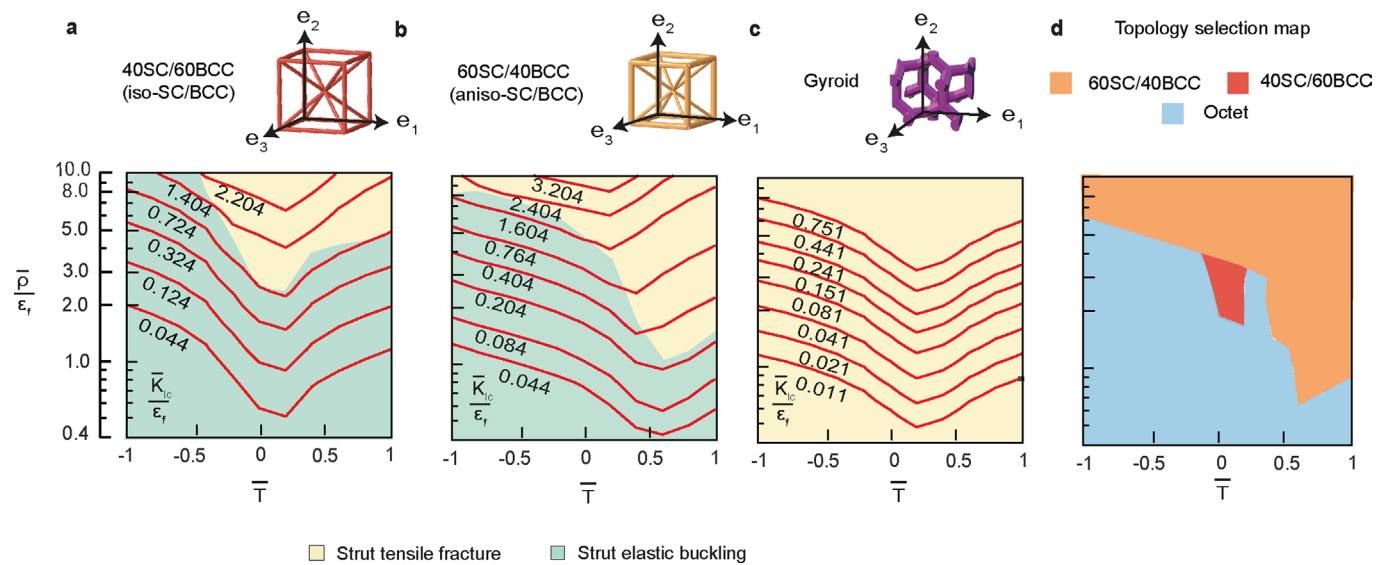
Reprints and permissions information is available at www.nature.com/reprints.



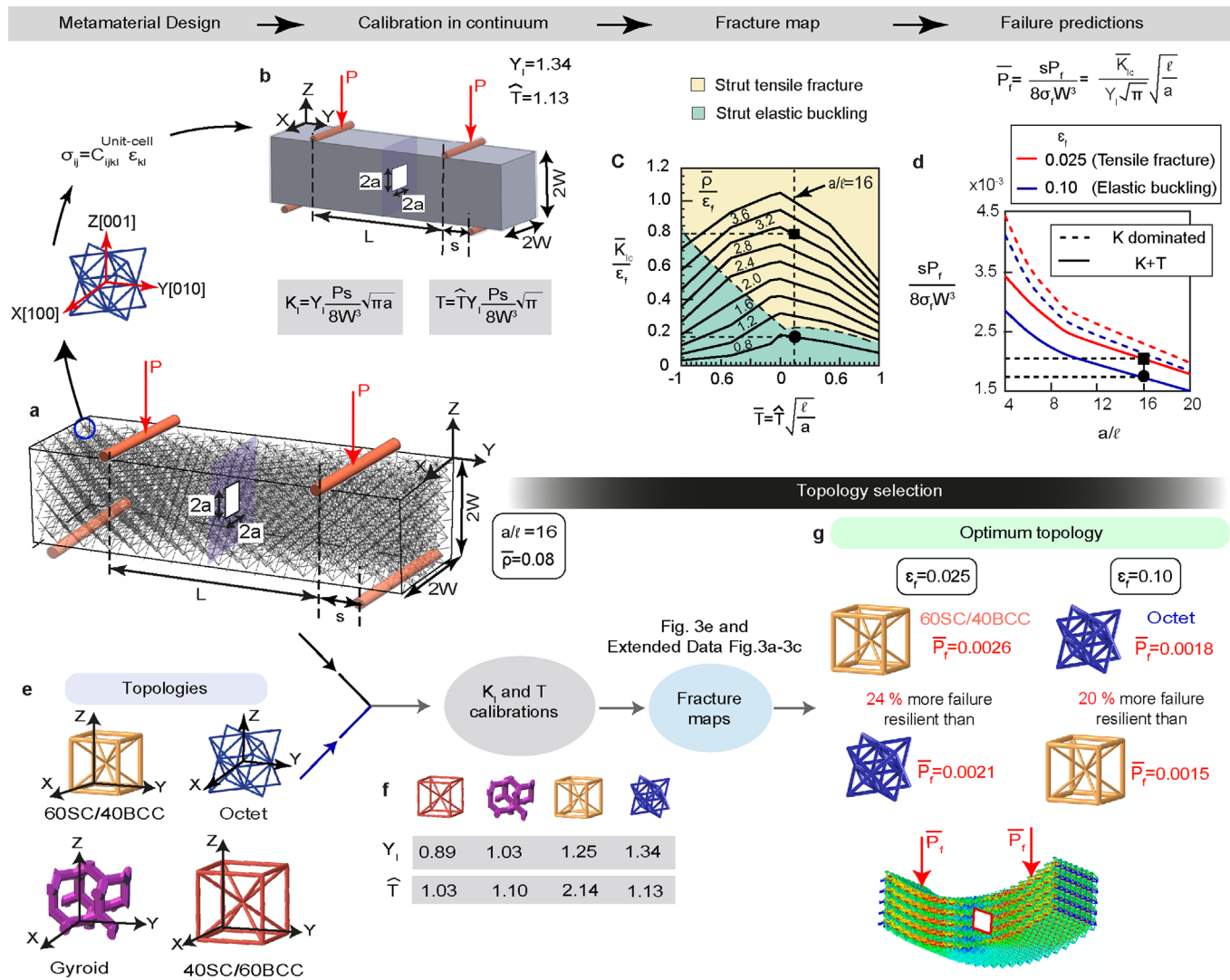
Extended Data Fig. 1 | Imperfection analysis. (a) CAD model for the $\bar{p} = 0.1$ specimen with strut diameter $2r_0 = 65 \mu\text{m}$ along with (b) an optical image of the printed specimen. (c) XCT image of the entire specimen comprising ~64,000 unit cells with the inset showing a more detailed view of a single unit cell within the specimen. (d) A magnified view of a larger region in the specimen in (c) with each location within the solid material shaded by the diameter D of the best-fit sphere at that location. (e) Probability density of diameters D within the entire specimen. The two modes correspond to best-fit spheres within the struts and node regions as marked. (f) The printed specimen was divided into 27 sub-cubes as shown, (g) cut and (h) then each individual cube was separately imaged via XCT to determine the distribution of the diameter D of the best-fit spheres as before. (i) The measured probability density function of D over the 27 sub-cubes is shown by the shaded zone with the solid line giving the mean over the 27 separate sub-cubes.



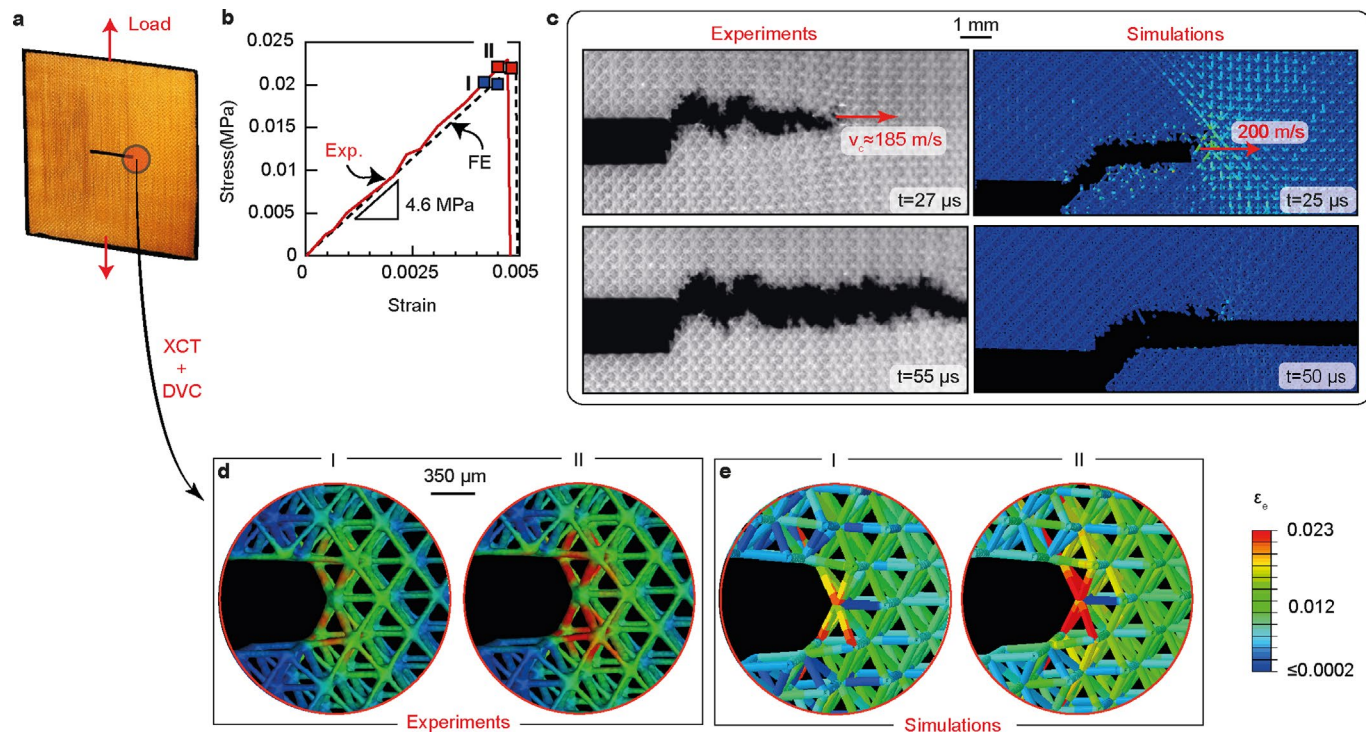
Extended Data Fig. 2 | Uniformity of mechanical properties. (a) Optical image of the printed specimen and (b) sketches depicting tensile testing along x , y and z - directions where z is the build direction. The measured tensile responses for the (c) $\bar{p} = 0.1$ and (d) $\bar{p} = 0.02$ specimens in the x , y and z -directions. Predictions based on the measured properties of a single strut (Supplementary Fig. 2) are included in (c) and (d). (e) The specimen cut into 27 sub-cubes and (f) uniaxial tensile tests were conducted on each cube along the (g) z - direction. The measured responses are shown in (h) and (i) for the $\bar{p} = 0.1$ specimen with two different choices of unit cell dimensions. The shaded zone depicts the variation over the 27 sub-cubes with the solid line the mean measured response.



Extended Data Fig. 3 | Fracture mechanism maps. Fracture mechanism maps of the stretch-dominated **(a)** isotropic compound simple cubic (SC) and body centered-cubic (BCC) truss **(b)** anisotropic compound SC/BCC truss **(c)** bend-dominated gyroid and **(d)** a topology selection map indicating which topology maximizes $\bar{K}_{IC}/\varepsilon_f$ in different regions of the $\bar{\rho}/\varepsilon_f$ versus \bar{T} space.



Extended Data Fig. 4 | Design with metamaterials. (a) Octet-truss beam of aspect ratio $L/W = 20$ with embedded crack ($a/W = 0.2$) subjected to four-point bending. (b) Geometry of the continuum anisotropic elastic beam used to determine the calibration factors Y_i and \hat{T} for K_i and T , respectively. (c) The cross-plotted fracture map from Fig. 3e. (d) Prediction of the normalized failure load \bar{P}_f of the $\bar{\rho} = 0.08$ octet-truss over a range of crack sizes and two choices of parent materials. The reference prediction for an assumed $\bar{\ell} = 0$ is also included. The black markers in (c-d) show examples of the prediction of the normalized failure load $P = P_f$ for a crack with $a/\ell = 16$ in a $\bar{\rho} = 0.08$ octet-truss metamaterial beam made from parent materials with $\epsilon_f = 0.025$ and 0.1. (e-g) Topology selection for maximizing failure load under four-point bending. (e) The four candidate topologies with their orientations labelled in the global beam co-ordinate system (X, Y, Z). (f) Continuum calibration of the geometric constants Y_i and \hat{T} and (g) description of the optimal topology and improvement over the next best candidate for a $\bar{\rho} = 0.08$ beam made from a parent material with failure strains $\epsilon_f = 0.025$ and 0.1.



Extended Data Fig. 5 | Fracture process zone and crack propagation. **(a)** Tensile loading of the $2B = 1\ell$ specimen ($a/\ell = 10$, $\bar{\rho} = 0.1$) and the corresponding **(b)** measurement and FE prediction of the tensile stress versus strain response. **(c)** High-speed photographs and corresponding FE predictions of crack propagation beyond peak stress with time $t = 0$ corresponding to the instant of the initiation of crack propagation at peak stress. **(d)** DVC measurements and **(e)** FE predictions of the distributions of the von-Mises strains ϵ_e within struts around the crack-tip. Measurements and predictions are shown at two load levels just prior to peak load marked in **(b)**. The scale bar is applicable for the strains in **c**, **d** and **e**.